On the universality of PIV uncertainty quantification by image matching

Andrea Sciacchitano[1], Fulvio Scarano[1] and Bernhard Wieneke[2]

[1] Aerospace Engineering Department, Delft University of Technology, Delft, The Netherlands
a.sciacchitano@tudelft.nl

[2] LaVision GmbH, Göttingen, Germany

ABSTRACT

The topic of uncertainty quantification in particle image velocimetry (PIV) is recognized as very relevant in the experimental fluid mechanics community, especially when dealing with turbulent flows, where PIV plays a prime role as diagnostic tool. The issue is particularly important when PIV is used to assess the validity of results obtained with computational fluid dynamics (CFD). An approach for PIV data uncertainty quantification based on image matching has been introduced by Sciacchitano *et al* [1], where the contribution of individual particle images to the correlation peak is analyzed and the uncertainty is retrieved from the ensemble of particle image disparities.

In this paper, the universality of the approach's working principle is investigated via the application to a wide gamut of experimental data of flows ranging from laminar to turbulent regime and from subsonic to supersonic. Also a methodology for evaluating the performance of the image-matching approach in different experimental conditions is proposed.

1   Introduction

Particle image velocimetry (PIV) is nowadays acknowledged as a standard diagnostic tool for fluid mechanics investigation. The topic of uncertainty quantification in PIV has received large attention since the dawn of the technique. Fincham and Delerce [2] distinguished two forms of error in PIV measurements, namely the *mean bias errors*, which mainly arise from the inadequacy of the discrete cross-correlation in evaluating the recordings, and the *random errors*, which result e.g. from background noise and in-plane and out-of-plane loss of pairs. A well-known example of bias error in PIV is the so-called *peak-locking* [3], which occurs when the particle image diameter is smaller than the pixel size; such error is due to the inadequacy of the three-point Gaussian fit [4] in evaluating the sub-pixel displacement. An additional form of error typical of PIV measurements is that associated to spurious vectors or *outliers*, which arise from erroneous correlation peak detection [5]. The error due to outliers is usually orders of magnitude greater than random and bias errors, therefore the detection of those is straightforward [6].

The investigation on PIV uncertainty quantification has been mainly conducted *a-priori* via theoretical modeling and/or Monte Carlo simulations. In the former case, theoretical models are proposed to describe the behavior of PIV interrogation and to quantify the effects of several error sources (e.g. displacement and displacement gradient) on the measurement precision [7], [8]. However, those models typically refer to simplified interrogation algorithms due to the complexity of modeling state-of-the-art multi-grid algorithms with window deformation. Monte Carlo simulations have been widely employed in literature to evaluate the performance of PIV interrogation algorithms [9], [10] because they allow complete control on flow and imaging parameters and a direct evaluation of the measurement error. However, it is acknowledged that numerical simulations lead to a major underestimate of the measurement errors due to the adoption of too idealized conditions. From the a-posteriori analysis, a typical figure of 0.1 pixels is obtained for the accuracy of PIV interrogation.

In contrast to the a-priori analysis, which provides only general information on the accuracy of PIV algorithms, *a-posteriori* uncertainty quantification allows estimating the uncertainty bounds for specific vector fields. This is required e.g. in industrial measurement campaigns where the experimental data are used for validation of CFD results. The topic of a-posteriori uncertainty quantification in PIV has received increasing attention in the last years. Nogueira *et al* [11], [12] proposed a multiple Δt strategy for the quantitative evaluation of peak locking errors. Timmins *et al* [13] introduced a method for automatic estimation of instantaneous local uncertainty, which relies on the errors obtained in numerical simulations

conducted with flow and imaging conditions similar to those of the real experiment. Such approach has the limitations of taking into account only a limit number of error sources and relying on numerical simulations which typically yield an underestimate of the measurement error. Wilson and Smith [14], [15] discussed the propagation of instantaneous errors to the errors on statistical quantities such as time average and Reynolds stress, which are of paramount interest in turbulence. More recently, Charonko and Vlachos [16] investigated an approach where the measurement uncertainty is quantified from the correlation signal-to-noise ratio. Such method showed good performance for robust phase correlation [17], while is not effective for standard cross-correlation. In the strain community, Wang *et al* [18] proposed an approach to quantify the uncertainty due to background Gaussian noise in the recordings.

Sciacchitano *et al* [1] investigated an uncertainty quantification methodology based on image matching. The basic idea of the approach consists in taking into account the contribution of individual particle images to the correlation peak and evaluating the positional disparity between paired particle images. In our previous work [1], the approach has been assessed via Monte Carlo simulations and on a water jet experiment. The aim of this paper is to prove the universality of the working principle by applying the method to different flow regimes considered representative of typical PIV measurements.

2   Background

2.1   Universality of the uncertainty quantification
As discussed in the introduction, several approaches for uncertainty quantification of PIV data have been proposed in the last years. These have been assessed mainly via Monte Carlo simulations and applied to a limited number of real experiments where the exact velocity field was known either from a more accurate measurement ([13], [14], [15]) or from fluid dynamics equations for simple cases of laminar flow [16]. However, such approaches have not been demonstrated to be *universal*, in the sense that they provide accurate uncertainty estimates in all the possible flow and imaging conditions encountered in typical PIV measurements. The present work introduces a methodology to show the universality of the image matching approach for uncertainty quantification.

To understand the rational of the *universality proof*, consider a generic measured quantity g affected by a measurement uncertainty u_g. In order to obtain indications on the measurement accuracy, the uncertainty is expressed in relative terms: $u_r \equiv u_g/g$. Contrarily to the absolute uncertainty u_g, the relative uncertainty u_r allows evaluating the goodness of a measurement and comparing the accuracy of different measurements, even when they refer to different physical quantities. When dealing with multiple measurements, e.g. in PIV where thousands of velocity vectors are measured in a 2D or 3D domain, or when the measurand is close to zero, the relative uncertainty is often computed as the ratio between the local absolute uncertainty and a reference quantity g_{ref}: $u_r \equiv u_g/g_{ref}$.

To evaluate the performance of the uncertainty estimator, the *error discrepancy* ε is defined as the absolute difference between actual measurement error δ, equal to the difference between exact and measured velocity, and the error $\hat{\delta}$ estimated with the image matching approach:

$$\varepsilon \equiv |\delta - \hat{\delta}| \tag{1}$$

Note that the computation of the error discrepancy ε requires the knowledge of the actual measurement error δ, which might be obtained as the difference between the measured velocity and the reference (or exact) velocity.

The fraction of vectors having error discrepancy below a certain value ε is indicated here as *population P(ε)*:

$$P(\varepsilon) \equiv 100 \times \frac{\text{number of vectors for which the error discrepancy is below } \varepsilon}{\text{total number of vectors}} \tag{2}$$

A point of the *P–ε* curve (Figure 1) indicates that for *P*% of the vectors the error discrepancy is below ε, while for the remaining (100–*P*)% it exceeds ε. Clearly these cumulative histograms strongly depend on the measurement: when the actual error is low (e.g. for uniform flows with negligible out-of-plane motion), low

values of the error discrepancy are expected; in contrast, in case of large actual errors (e.g. for turbulent flows), most of the vectors are foreseen to have large error discrepancy. Two measurements are considered in Figure 1, having rms errors of 0.05 pixels and 0.15 pixels, respectively. In the first measurement, more than 80% of the total vectors have error discrepancy $\varepsilon \le \varepsilon_{Thr} = 0.05$ px (where ε_{Thr} is arbitrarily chosen), while in the second one the percentage is reduced to about 30%.

In order to evaluate the goodness of the error estimator comparing results from different measurements, the error discrepancy is normalized with respect to a reference error, similarly to what is done for the relative uncertainty:

$$\varepsilon^* \equiv \frac{|\delta - \widehat{\delta}|}{\delta_{Ref}} \tag{3}$$

A point of the P–ε^* indicates that P% of the vectors have relative error discrepancy below ε^*, while the remaining $(100–P)$% have relative error discrepancy above ε^*. Figure 2 shows that an appropriate choice of δ_{Ref} makes the population curves fall on top of each other; now approximately the same percentage of vectors $(P_1 \cong P_2)$ have relative error discrepancy below the threshold value ε^*_{Thr}. This means that the error estimator has similar performance when applied to the two measurements, even if they exhibit different values of the actual error. When this test is conducted for several different measurements representative of typical PIV experiments and the population curves fall on top of each other, the *universality* of the error estimator is proved.
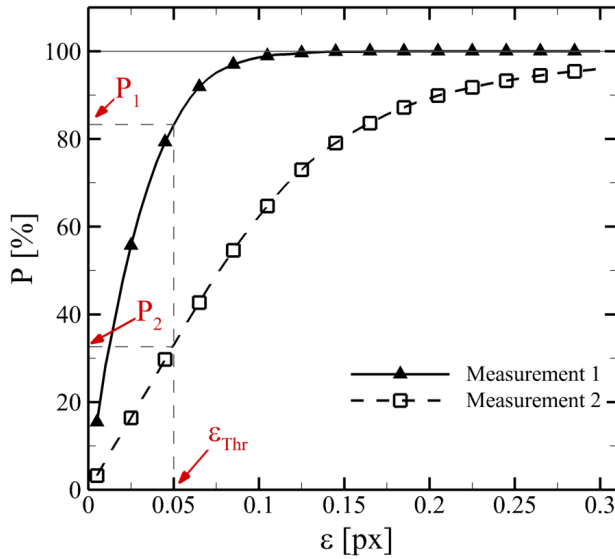

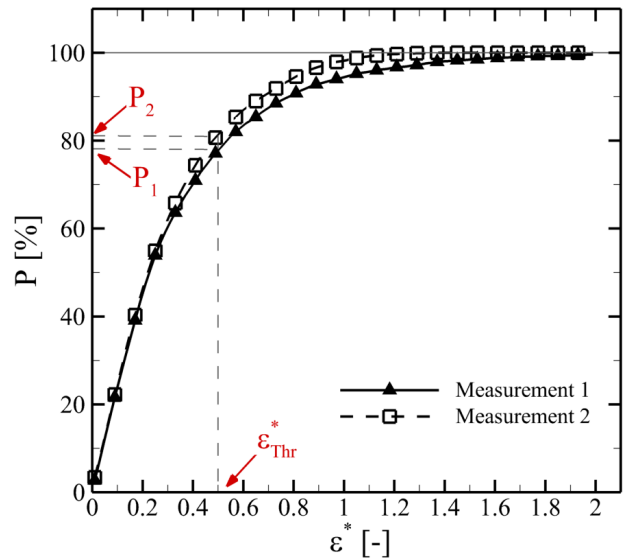Figure 1. Cumulative histograms of the error discrepancy.

Figure 2. Cumulative histograms of the relative error discrepancy.

2.2 Working principle of the uncertainty quantification by image matching

This work investigates the universality of the image-matching uncertainty estimator introduced by Sciacchitano *et al* [1]. A detailed description of the estimator's working principle and implementation is reported in the paper mentioned above [1]. Here a brief summary of the key points is reported.

    a. *Image matching.* The measured velocity is used as a predictor to match the particle images at the best of the velocity estimator.

    b. *Particle image pair detection.* Particle images occurring in both exposures and falling close to each other are detected as a pair.

    c. *Disparity vector computation.* The distance between the particle image pair is evaluated with sub-pixel accuracy.

d. *Statistical analysis of the disparity vector ensemble.* The velocity vector uncertainty is retrieved from the mean value and the statistical dispersion of the disparity vector within the interrogation window.

3   Setup of the experiments

3.1   Methodology

Exposures of a set of particle images are recorded by a PIV system, here referred to as the *measurement system*, in conditions similar to a typical experiment. These images are processed with the LaVision DaVis software and yield the *measured displacement field*, whose uncertainty is quantified via the image matching approach.

The performance of the uncertainty quantification via image matching is evaluated by direct comparison with the *true measurement error*, which here is obtained in two different ways:

1. *Spectral analysis.* For time resolved measurements conducted with a single camera, the velocity amplitude spectrum is computed in a measurement point. According to turbulence dynamics, energy is transferred from large time-scale eddies to small time-scale eddies and then dissipated by viscosity at the Kolmogorov time scale [19]. Hence, for sufficiently high frequency, the energy content decreases for increasing frequency. However, the presence of measurement noise, which has high frequency content because mainly uncorrelated in time, prevents the measured spectrum from going toward zero. As proposed by Ghaemi *et al.* [20], the minimum value of the measured energy spectrum is here employed to determine the measurement noise level.

2. *Concurrent measurements.* An additional PIV measurement system, here called the *high-dynamic range* (*HDR*) *system*, is used in the acquisition phase. Such system records the exposures in optimal imaging conditions (mean particle image diameter about 2.5-3 pixels according to [21], quantization level of 12 bits) and at higher velocity dynamic range (magnification factor typically 3 to 4 times higher than for the measurement system). Even assuming the same absolute error as in the measurement system, an increase by 3 to 4 times of the dynamic velocity range DVR [22] is achieved. However, since the HDR measurement is conducted in *"optimal"* conditions, the DVR gain typically exceeds factor 5. The displacement field retrieved with the HDR system can thus be regarded as a *reference* (or *exact*) *displacement field*, because it yields measurement errors at least five times below those of the *measured displacement field*. Finally the *actual error* is computed as the difference between measured and reference displacement field and is compared to the estimated uncertainty to investigate the performance of the image matching approach.

Several flow fields considered representative of typical PIV experiments have been selected for the test; the main features of the experiments are reported in Table 1.

Table 1. Description of the experiments

Experiment	Re [-] or Mach [-]	Wind tunnel	Type of analysis
Shear layer	Re = 12,000	V-tunnel	Concurrent measurements
Turbulent wake behind a prism	Re =100,000	V-tunnel	Spectral analysis
Uniform transverse flow	V_∞ = 2.1 m/s	V-tunnel	Concurrent measurements
Supersonic boundary layer	M = 2.0	ST-15	Concurrent measurements

3.2 Experimental apparatus

3.2.1 Subsonic experiments

The subsonic experiments are conducted in the vertical wind tunnel located at the Aerodynamics Laboratories of Delft University of Technology. The wind tunnel has an open test section with circular cross-section of 60 cm diameter. The contraction ratio of 150:1 yields a turbulent intensity of about 0.02 % at free stream velocity of 10 m/s.

A dual cavity diode pumped Nd:YLF laser (Litron Lasers, LDY303HE) provides light at wavelength $\lambda = 527$ nm. Each cavity delivers a pulse energy of 22.5 mJ/pulse at 1 kHz. The laser beam has an output diameter of 3 mm and is shaped into a sheet approximately 2 mm thick using spherical and cylindrical lenses. Seeding particles of mean diameter $d_p = 1$ µm are generated by a SEFEX smoke generator and dispersed in the settling chamber. Images of the seeding particles are recorded by two Photron Fast CAM SA1 cameras, having 12-bit CMOS sensor of 1024×1024 pixels (pixel pitch of 20 µm). The cameras are equipped with Nikon objectives of focal length 105 mm and 200 mm respectively.

3.2.1.1 Shear layer experiment

The flow around a prism of rectangular base 4×6 cm^2 (W×H) and spanwise length L = 70 cm is investigated. The free-stream velocity is set to $V_\infty = 3.6$ m/s, yielding a Reynolds number $Re_H = 12,000$ based on the prism height. Images are recorded in continuous mode at $f_{acq} = 5,000$ Hz. The fields of view of the measurement and HDR systems (FOV$_M$ and FOV$_H$, respectively) are 2.0W×2.0W and 0.7W×0.7W, respectively (Figure 3); the magnification factors equal $M_M = 0.25$ and $M_H = 0.74$, respectively. The origin of the coordinate system $(x_0,y_0) = (0,0)$ is chosen at the bottom left corner of the base. The recordings are processed with LaVision Davis 8.1, which makes use of a multi-grid iterative interrogation algorithm with window deformation based on WIDIM [9]. Gaussian weighted interrogation windows are selected with size of 16×16, 32×32 and 64×64 pixels respectively. The overlap factor is kept constant to 75% for each interrogation window.
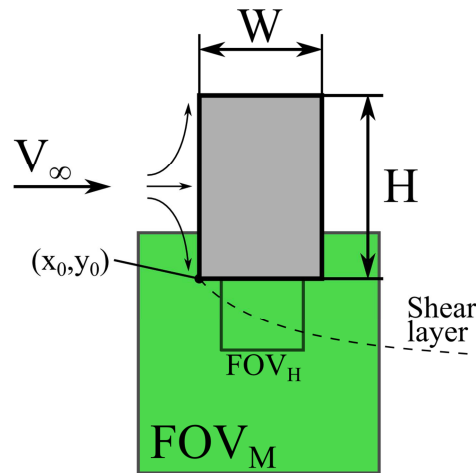

Figure 3. Fields of view of the measurement and HDR systems.

3.2.1.2 Turbulent wake behind a prism

The same model as in section 3.2.1.1 is used for the present test case. The analysis is conducted with only one PIV system (i.e. the *measurement system*) imaging a field of view of 18.5×18.5 mm^2 centered along the base centerline 4.5 W downstream of the prism (Figure 4). In order to achieve an acquisition frequency $f_{acq} = 10,000$ Hz, the active region of the sensor is reduced to 256×256 pixels. The optical magnification equals M = 0.28. The free-stream velocity is chosen equal to $V_\infty = 24$ m/s, yielding a Reynolds number of about 100,000 based on the model's height.
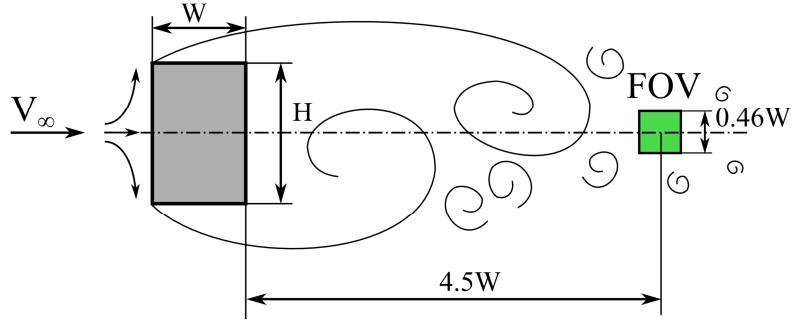
Figure 4. Field of view of the turbulent wake experiment.

The recordings are processed with LaVision Davis 8.1 using Gaussian weighted interrogation windows of size 16×16, 32×32 and 64×64 pixels respectively with 75% overlap factor.

3.2.1.3   *Uniform transverse flow*

The effect of the through-plane motion is investigated in the present experiment. The wind tunnel is run at free-stream velocity $V_\infty = 2.1$ m/s without any model mounted in the test section. The laser sheet has a thickness $\Delta z = 2$ mm and is tilted of $\alpha = 9$ deg with respect to the free-stream direction. Hence, the free-stream velocity has a component $V_{\infty\perp}$ orthogonal to the laser sheet which causes a through-plane particle displacement (Figure 5); the latter can be regulated through the pulse separation time δt. The sensor size of the two cameras is cropped to 512×512 pixels to achieve an acquisition frequency of $f_{acq} = 10,000$ Hz in continuous mode, yielding a through plane displacement $w_0/\Delta z = 0.016$. Larger through-plane displacements (multiples of $w/\Delta z = 0.016$) are obtained by skipping recordings in time; for example, when the first image is correlated with the fourth one, the out-of-plane displacement equals $3 \cdot w_0 = 0.048\Delta z$.

The measurement camera mounts a Nikon objective with 105 mm focal length, while for the HDR camera the objective's focal length is 200 mm. The f-number is set to 4.0 for both cameras. The fields of view of HDR and measurement system are 10.6×10.6 mm² and 40.5×40.5 mm² respectively, yielding magnification factors $M_H = 0.97$ and $M_M = 0.25$.
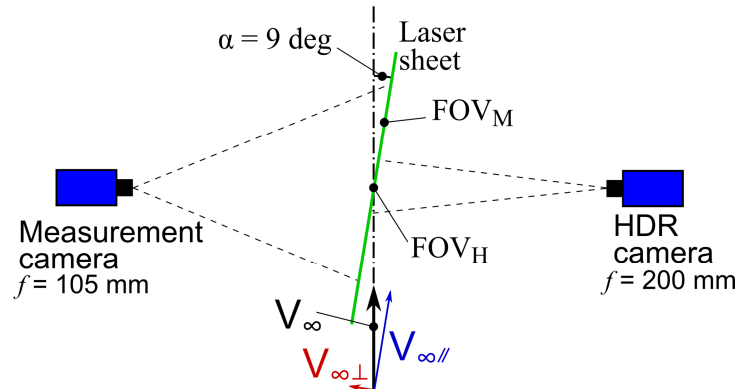

Figure 5. Experimental setup for the uniform transverse flow experiment.

3.2.2   **Supersonic experiment – Supersonic boundary layer**

Supersonic experiments are performed in the ST-15 wind tunnel of the Aerodynamics Laboratories of Delft University of Technology. The wind tunnel has a test section of 150×150 mm² and is operated at Mach 2.0 and total pressure $p_0 = 3.1$ bar.

Planar PIV experiments are conducted to investigate the boundary layer generated at the wind tunnel's wall. The flow is seeded with micron size di-ethyl-hexyl-sebacate (DEHS) particles, having a nominal median diameter of $d_p = 1$ μm. Experiments conducted by Ragni *et al* [23] showed a typical relaxation time of 2 μs of such particles in a Mach 2.0 flow. The seeding particles are injected into the flow in the settling chamber.

The particle tracers are illuminated by a Quantel CFR PIV-200 laser (double-pulsed Nd:YAG laser, with 200 mJ pulse energy and 9 ns pulse duration at 532 nm wavelength). Laser optics are used to shape the laser

beam into a plane of 1 mm thickness along the span. Images are recorded by two PCO Sensicam QE cameras having CCD sensors with 1376×1040 pixels, pixel pitch of 6.45 μm and 12-bit quantization level. The sensor is cropped to 320×800 pixels in the streamwise and vertical directions respectively to achieve an acquisition rate of 10 Hz in double-frame mode. The pulse separation time is set to 0.6 μs.

The measurement camera is equipped with a Nikon objective of focal length 60 mm and images a region of 15.3×38.2 mm (magnification factor $M_M = 0.14$); a 105 mm focal length Nikon objective is mounted on the HDR camera, which images a region of 4.0×10.0 mm (magnification factor $M_H = 0.52$, Figure 6). The f-number is set to $f\# = 11$ and $f\# = 16$ for the two cameras, respectively.

The recordings are processed with LaVision DaVis 8.1, using interrogation windows of 64×64 pixels for the HDR camera and 16×16 pixels for the measurement camera, both with Gaussian weighting and 75% overlap factor. Due to the difference in the magnification factor, the selected processing parameters yield velocity fields that have approximately the same spatial resolution for measurement and acquisition system.
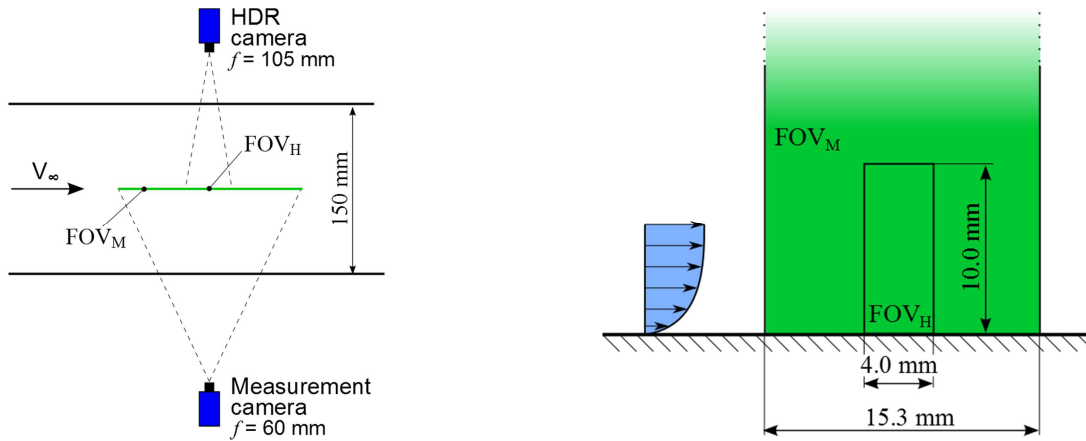

Figure 6. Measured and HDR fields of view (FOV$_M$ and FOV$_H$, respectively) for the supersonic boundary layer experiment; top view (left) and side view (right).

4   Results

4.1   Shear layer

A shear layer originates at (0,0) which divides the outer flow from the separated region adjacent to the prism edge (left of Figure 7). In the separated shear layer, vortices are periodically formed due to the Kelvin-Helmotz instability; the frequency of formation of the vortices is determined from visual inspection and corresponds to Strouhal number $St_H = 3.5$, which agrees with the value measured by de Kat *et al.* [24]. In the outer region the flow is laminar and low velocity fluctuations are found (below 0.5 pixels, Figure 7 right); the fluctuation level is higher in the separated region (about 1 pixel) where the flow is turbulent. The largest velocity fluctuations (exceeding 3 pixels) occur at the shear layer location and are associated to the vortex formation and the flapping motion of the shear layer. The maximum fluctuations take place downstream the location x = 300 px (x/W = 0.6) due to the transition from laminar to turbulent regime.
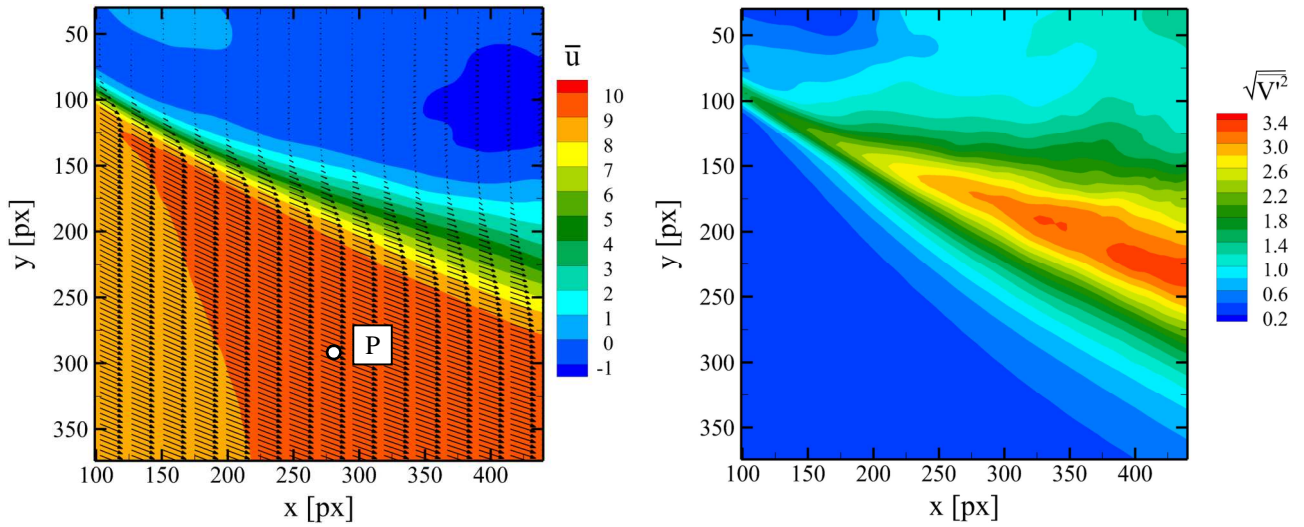
Figure 7. Left: reference mean horizontal velocity with velocity vectors (for sake of clarity, one every 6 vectors is displayed in the x-direction). Right: reference fluctuations root mean square. Both quantities are expressed in pixels.

Figure 8 shows the time series of measured and reference velocity (i.e. velocity measured by the HDR system) in a point P in the outer region. The plots evidence that the measured velocity is affected by random noise that yields high-frequency spurious fluctuations. In contrast, the reference velocity exhibits only low-frequency fluctuations associated with the vortex shedding phenomenon.
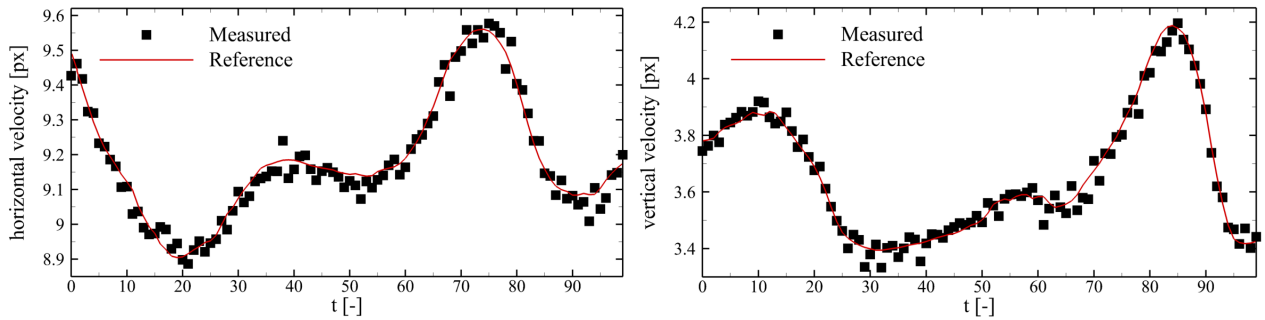

Figure 8. Time series of horizontal velocity component (left) and vertical velocity component (right). Full squares: measured velocity; continuous line: reference velocity.

Three error sources are predominant in the present test case: first, the velocity gradient in the shear layer, which reaches 0.2 pixels per pixel (Figure 9 left); second, the curvature of the streamlines due to the Kelvin-Helmotz vortices (Figure 9 right); finally, the out of plane motion downstream of the transition point. These error sources are major along the shear layer, while they are small in the outer flow region, where significantly lower errors are expected.
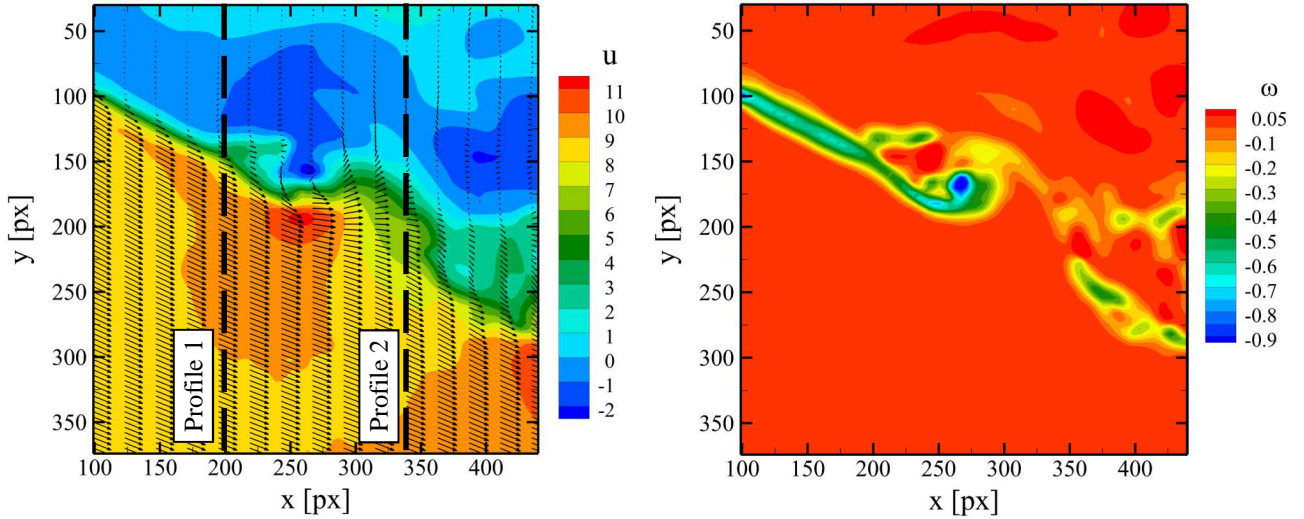
Figure 9. Left: instantaneous horizontal velocity. For clarity, the vectors are displayed every 6 in x-direction. Right: instantaneous vorticity field. The velocity is expressed in pixels, the vorticity in arbitrary units.

The error magnitude along two profiles is computed as the root-mean-square of the error time series (Figure 10); the former profile is located in the laminar regime (x = 200 px), while the latter is beyond transition (x = 340 px). In the laminar profile, the measurement error exhibits a clear peak at the mean shear layer location (y = 150 px), which suggests that the error is primarily due to in-plane velocity gradients. The estimated peak value is in good agreement with the actual value (0.2 pixels). In the separated region and the outer flow, the low velocity gradients cause the measurement error to drop significantly down to 0.03 pixels. As already stated in our previous work [1], the image matching approach overestimates errors below a *"fog level"* (typically 0.05 pixels), which represents the sensitivity of the algorithm and is related e.g. to the image interpolation algorithm and the particle image peak detection.

Beyond transition, the amplitude of the shear layer flapping motion increases, resulting in high velocity fluctuations spread over a larger region. Also at this location, the measurement error peak is found where the velocity fluctuations are the highest. In this case, the measurement error is primarily due to the streamlines curvature and to three-dimensional turbulent motion. As a consequence of the larger amplitude of the shear layer flapping motion, the error peak broadens (Figure 10, right). The image matching approach correctly reproduces the broadening of the mean error peak; however, the peak value is underestimated of 25%. In the separated region and the outer flow, the same considerations as before apply: the error is overestimated because it lies below the fog level.
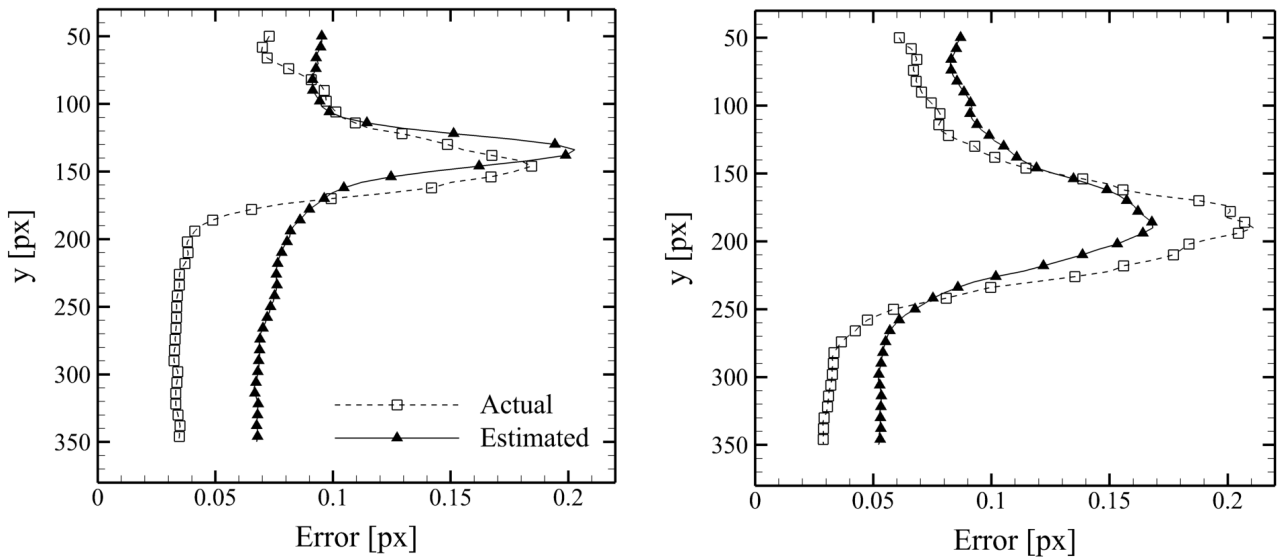

Figure 10. RMS error profiles at x = 200 pixels (x/W = 0.4, left) and x =340 pixels (x/W = 0.68, right). For clarity, one every two samples is displayed.

To evaluate the agreement between instantaneous actual and estimated errors, the cross-correlation coefficient ρ between the two quantities is computed [25]. Such parameter equals 1 if δ and $\hat{\delta}$ are linearly dependent, while it is null when they are uncorrelated. The contour plot of Figure 11 shows that where the measurement error exceeds the fog level, that is in the shear layer and in the separated region, the cross-correlation coefficient typically exceeds 0.2 with peaks up to 0.6. The error time series extracted from point A (Figure 11 top-right) evidences the presence of error peaks ascribed to out-of-plane motion or small vortices not accurately reproduced by the measurement system. In contrast, values of ρ approaching zero are found in the outer region because here the measurement error falls below the fog level; as it is illustrated in the time series of point B (Figure 11 bottom-right), in this case the image matching approach overestimates the error.
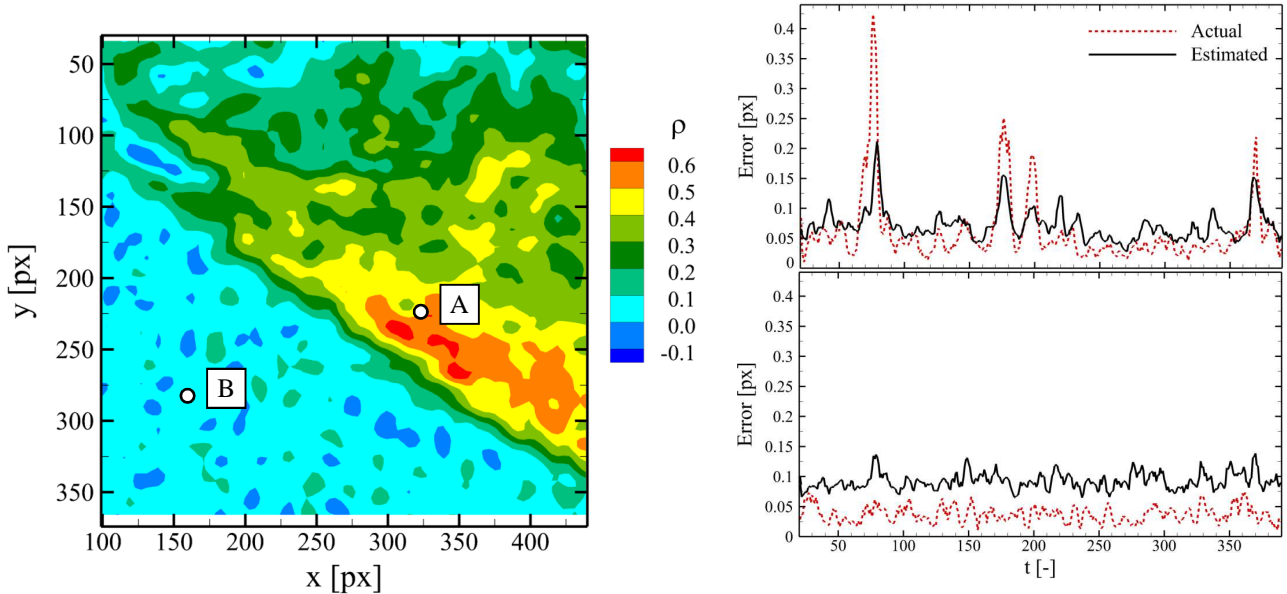

Figure 11. Left: cross-correlation coefficient between actual and estimated error. Right: error time series in A (top) and B (bottom).

4.1.1 Effect of the particle image diameter

The particle image diameter is known to affect the accuracy of PIV measurements. Theoretical models and numerical simulations ([7], [21]) evidence that the measurement error is minimized for particle image diameters between 2 and 3 pixels. Smaller particle images yield systematic errors known as *peak locking* [3], ascribed to the inadequacy of three-point Gaussian fit to accurately estimate the sub-pixel displacement. In contrast, large particle images lead to increased uncertainty in the determination of the particle centroid.

A common practice to mitigate peak locking errors consists in slightly translating the focal plane with respect to the measurement plane [26], so that the particles are imaged slightly out of focus and their diameter increases in the recordings. However, it is not clear whether such practice also increases the random component of the error.

In this section, three sets of recordings of the shear layer flow are analyzed, with particle images correctly in focus (mean diameter $d_\tau = 1$ pixel), slightly out of focus ($d_\tau = 2.5$ pixels) and strongly out of focus ($d_\tau = 3.5$ pixels) respectively, see Figure 12. In the former case the peak locking is severe (degree of peak locking $C = 0.4$, according to [26]), while it is dramatically reduced when the particles are out of focus (C below 0.15 in both sets 2 and 3).
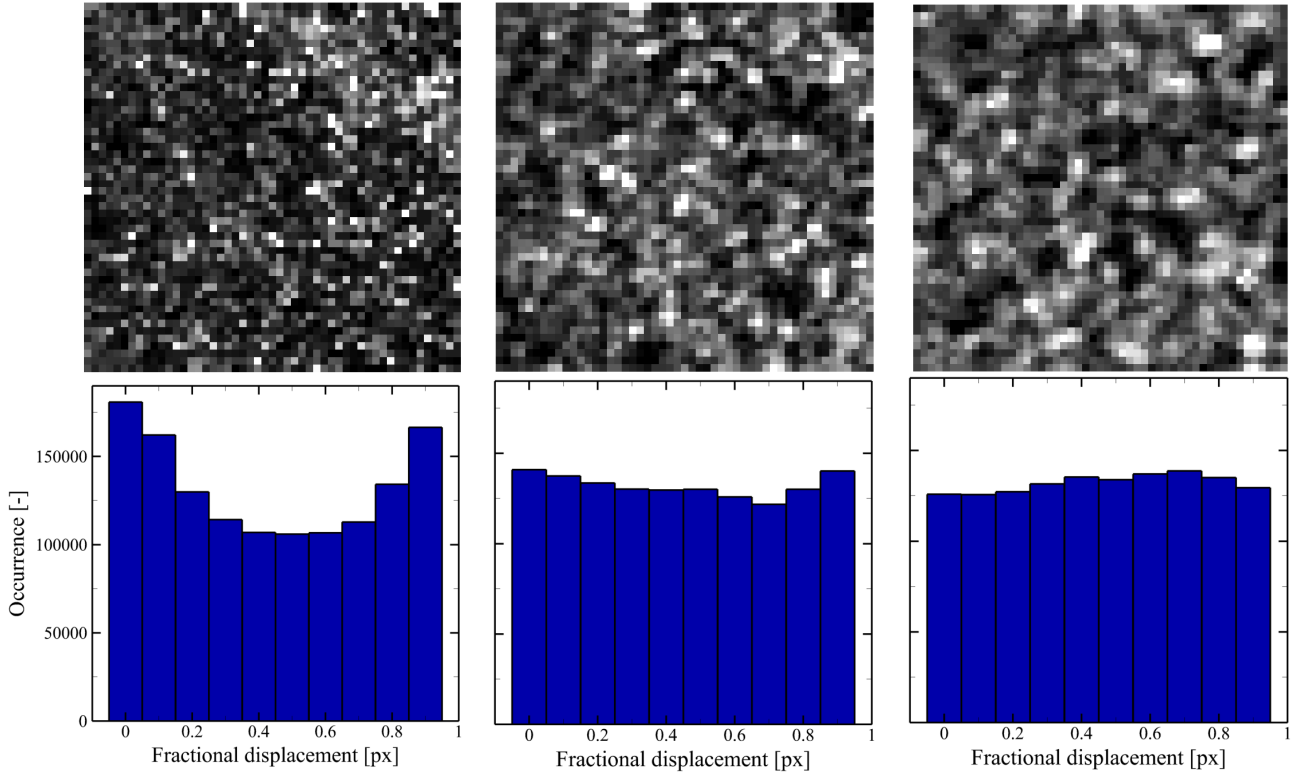
Figure 12. Details of the acquired recordings (top row) and corresponding fractional displacement histograms (bottom row). From left to right, set 1, 2 and 3.

The error profiles of Figure 13 evidence the effects of the image defocusing on the measurement accuracy. The peak errors obtained with particles in focus and slightly out of focus ($d_\tau = 1$ and 2.5 pixels, respectively) are comparable and are estimated within 30% by the image matching approach. In the outer region, the measurement errors drop significantly and a large difference is noticed between the two measurement sets, with the latter yielding an error reduction by factor 2 with respect to the former, which is ascribed to the reduction of peak locking errors due to the defocusing practice. In this region, the error is typically overestimated when it falls below a fog level of about 0.05 pixels.

The third set (recordings strongly out of focus, mean particle image diameter $d_\tau = 3.5$ pixels) exhibits increased measurement errors both in the shear layer and in the outer region due to the higher uncertainty in determining the particle image centroid. The peak error is correctly estimated by the image matching approach, while the estimated error in the outer region does not drop below 0.1 pixels, which suggests that the fog level depends on the particle image diameter. This occurs because large particle images are more sensitive to noise in the recordings, therefore the location of the particle image centroid with the three-point Gaussian fit becomes more uncertain. A singnificant enhancement of the particle image location detection and therefore of the uncertainty estimation for large particle images is expected with a more advanced particle position detector, e.g. a two-dimensional 5×5 Gaussian fit [27]. Such improvement of the image matching algorithm for uncertainty quantification is left to future work.
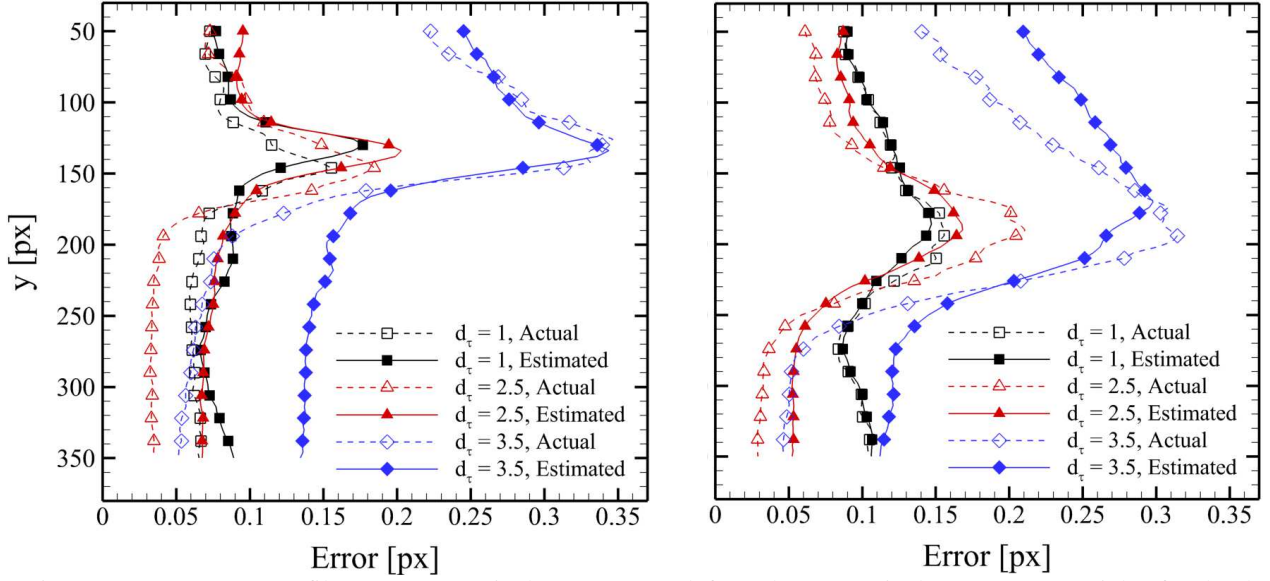
Figure 13. RMS error profiles at x = 200 pixels (x/W = 0.4, left) and x =340 pixels (x/W = 0.68, right) for the three different sets of measurement. For clarity, one every four samples is displayed.

4.2   Turbulent wake behind a prism

The turbulent flow at Reynolds number Re_H = 100,000 has been selected due to the wide range of length and time scales present. An instantaneous contour of $Q = \dfrac{\partial u}{\partial x}\dfrac{\partial v}{\partial y} - \dfrac{\partial u}{\partial y}\dfrac{\partial v}{\partial x}$ [28] is depicted in Figure 14 to illustrate the presence of small-scale vortical structures having wavelength λ below 50 pixels. Figure 15 shows a portion of the horizontal velocity time series extracted in a point P of coordinates $(x,y) = (130,130)$ px. Considering the entire sequence of velocity fields, the mean and standard deviation of the horizontal velocity equal $u_{mean} = -0.94$ px and $u_{std} = 0.98$ px respectively.
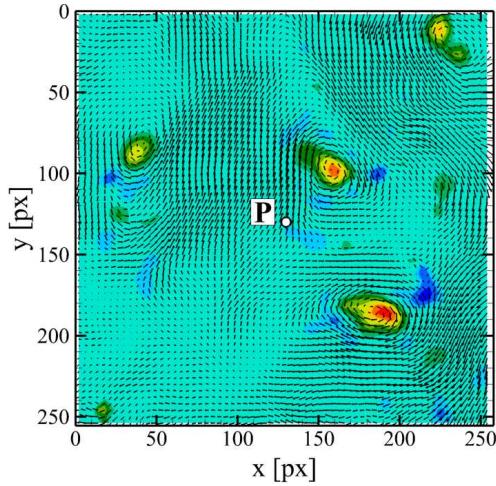

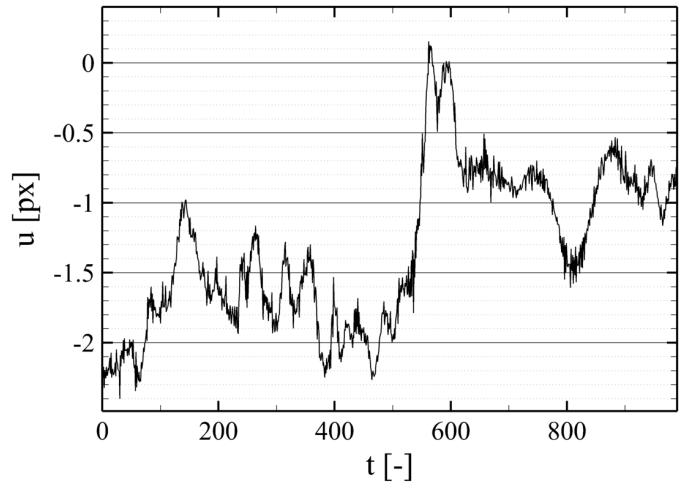Figure 14. Instantaneous value of Q and velocity vectors relative to the convective velocity.

Figure 15. Horizontal velocity time series in x = 130 px and y = 130 px.

The Eulerian linear spectral density (LSD) of the horizontal velocity in P is computed for the three interrogation window sizes.

From turbulence dynamics, the amplitude spectrum (viz. LSD) can be divided into three different regions [19]. The *large-scale sub-range* is characterized by low frequency fluctuations (in the experiment below 60 Hz), where the viscous effects are negligible and energy is transferred from the mean flow to small scales. In the *inertial sub-range*, no energy is added by the mean flow and no energy is taken out by viscous dissipation; in contrast, energy is transferred from low to large frequencies. Finally, in the *viscous sub-range* the energy is dissipated by viscosity.

In the ideal case of large Reynolds number and no measurement noise, the time spectrum is approximately constant in the large-scale sub-range, it monotonically decreases in the inertial sub-range and it is null in the viscous sub-range (Figure 16).
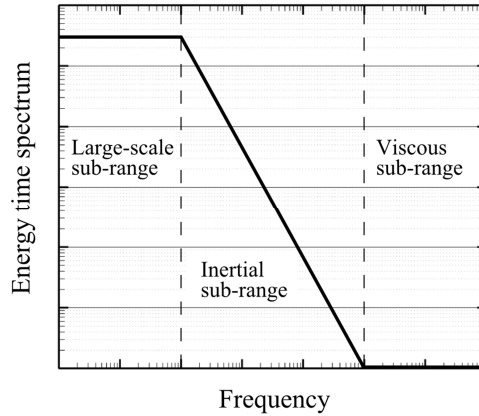

Figure 16. Eulerian energy time spectrum in the ideal case of large Reynolds number and no measurement noise.

In the real case, high frequency fluctuations are present due to measurement noise and the LSD reaches a positive minimum value which equals the noise level, as shown in the plots of Figure 17; in these plots, the value of the LSD is multiplied by the square root of the frequency so that the vertical axis of the plots indicates the amplitude (in pixels) of the velocity fluctuations.

The plot for widow size of 16×16 pixels (Figure 17 left) exhibits an amplitude distribution varying over one decade up to a frequency of approximately 700 Hz; the measurement noise obtained from the linear spectrum is 0.048 pixels. In addition to the indication of the time spectrum, the measurement error is also evaluated with the image matching approach, obtaining an estimated value of 0.080 pixels. Increasing the interrogation window size to 64×64 pixels yields a major reduction in both the actual and the measured error due to the increase in the correlation signal strength. In this case, the amplitude distribution varies over one decade and a half up to a frequency of 1,000 Hz.
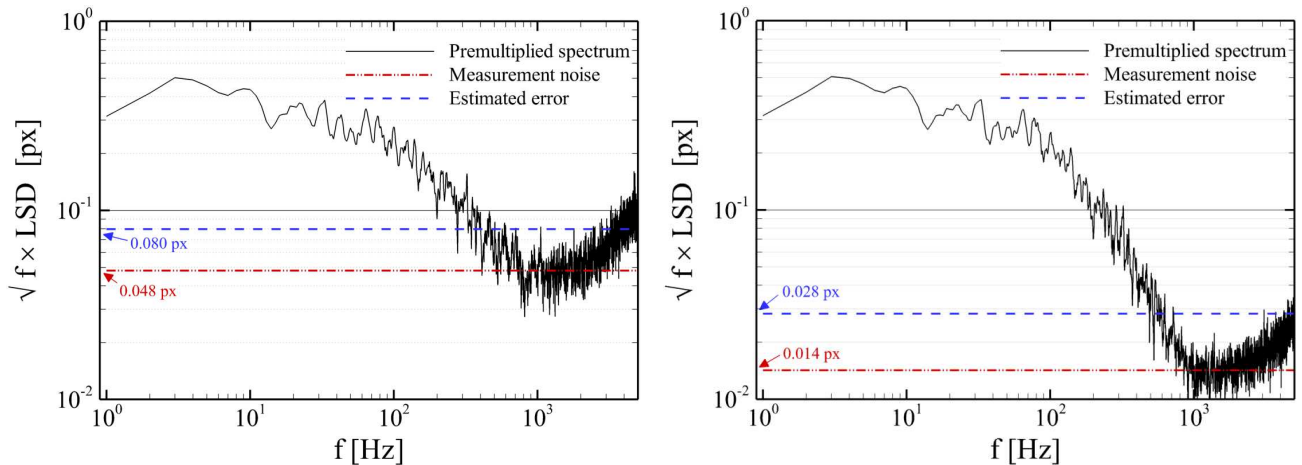

Figure 17. Pre-mulitplied LSD of the horizontal velocity in P. Left: 16×16 px; right: 64×64 px.

Figure 18 summarizes the measurement errors for different interrogation window sizes. As discussed in our previous work ([1]), the error is inversely proportional to the linear window size, i.e. it scales with the square root of the number N of particle image pairs. The results of Figure 18 prove the validity of the proposed model. However, the image-matching approach yields an overestimate by up to factor two of the measurement error with respect to the value obtained with the spectral analysis.

An additional approach for error estimation is analyzed here, already employed by Violato and Scarano [29]. In such approach, a second-order polynomial least-square regression is applied to the velocity time series over a time kernel smaller than the typical time scales (here 11 time steps). The measurement error is

estimated as the residual of the difference between velocity time history and polynomial regression. Such approach can be applied whenever time-resolved data are available and, as illustrated in Figure 18, it provides accurate estimates of the measurement error under the condition that the latter is mainly uncorrelated in time.
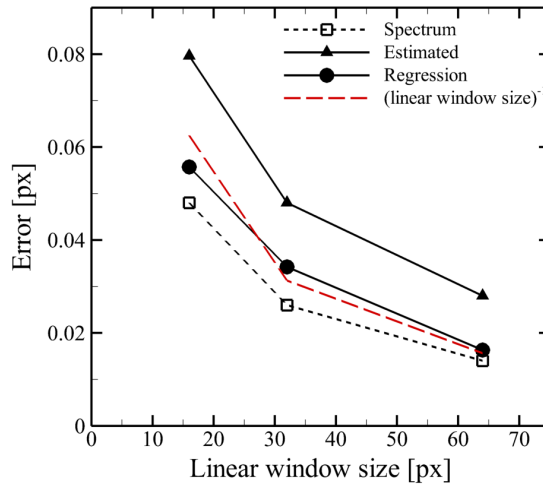

Figure 18. Measurement error as a function of the interrogation window size.

4.3   Uniform transverse flow

The contribution of the out-of-plane motion to the measurement error is well documented in literature ([21], [22], [30], among others). The seeding particles motion thorugh the light sheet causes variations of the imaged intensity level; in presence of overlapping particle images, the relative variation of intensity yields a biased displacement estimate. Furthermore, the out-of-plane motion leads to loss-of-pairs which lessens the correlation peak strength. The resulting error is of the order of 0.1 pixels and is reported to increase exponentially with the through-plane displacement [30]. This behavior is also retrieved in the present experiment (Figure 19), where the estimated error matches the actual error within 35% of its value. Also, the total error decreases when increasing the interrogation window size from 16×16 pixels 32×32 pixels due to the larger number of particle image pairs that strengthen the correlation signal.
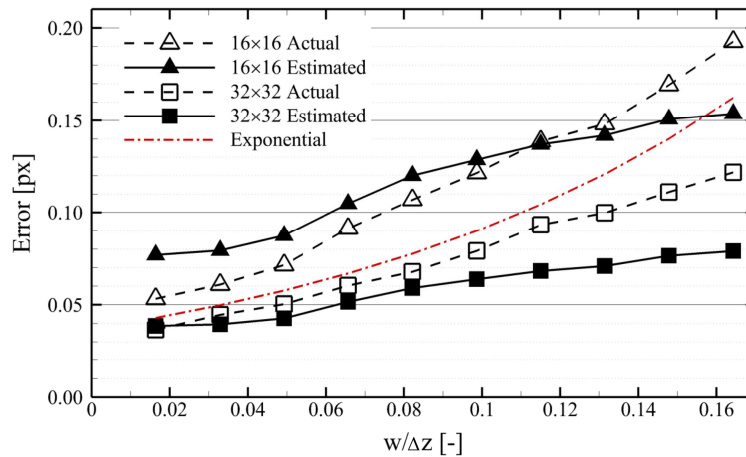

Figure 19. RMS error as a function of the out-of-plane displacement.

4.4   Supersonic boundary layer

The boundary layer develops for a length of approximately 1 m on a surface under nearly adiabatic conditions, reaching a thickness of $\delta_{99} = 5.5$ mm. The characteristics of the boundary layer are evaluated using the recordings from the HDR system. The incompressible displacement thickness δ^* and the incompressible momentum thickness θ equal 0.67 mm and 0.52 mm respectively, yielding an incompressible shape factor H_{inc} of 1.29. The Reynolds number based on the incompressible momentum thickness is

$Re_\theta = 21,000$. The skin friction coefficient C_f is computed with the Van Driest II formula in combination with the Crocco-Buseman relation [31] with recovery factor $r = 0.89$ and equals 1.8×10^{-3}; the corresponding friction velocity is $u_\tau = 19.7$ m/s. The parameters of the supersonic boundary layer experiment are reported in Table 2; the results are in good agreement with previous experiments conducted by Sun *et al* [32].

Table 2. Supersonic boundary layer parameters.

Parameter	Value
M_∞ [-]	2.0
u_∞ [m/s]	501
p_0 [Pa]	3.1×10^5
T_0 [K]	285
δ_{99}[mm]	5.5
δ^*[mm]	0.67
θ [mm]	0.52
H_{inc} [-]	1.29
Re_θ [-]	21,000
C_f [-]	1.8×10^{-3}
u_τ [m/s]	19.7

Figure 20 shows the boundary layer profile expressed in inner units $u^+ = u/u_\tau$ and $y^+ = y\,u_\tau/\nu$, being ν the fluid kinematic vicosity at the wall. The reference profile and the measured one are plotted for comparison. The reference profile follows the log law ($u^+ = \frac{1}{0.41}\ln(y^+) + 5.0$, [31]) in the range $60 < y^+ < 2,000$, which corresponds to $0.01 < y/\delta_{99} < 0.32$. The linear sublayer (where $u^+ = y^+$) is not visible in the present experiment due to the limited spatial resolution of PIV. For $y^+ > 2000$, the reference profile departs from the log law due to a mild adverse pressure gradient in the outer region (wake component, [31]). The measured boundary layer profile falls on top of the reference one for $y^+ \geq 200$ ($y/\delta_{99} \geq 0.03$); this result suggests that the present experiment is free of major systematic error sources. The measurement point closest to the wall is in $y^+ = 90$; such data departs from reference profile and log law due to the limited spatial resolution of the measurement system.

The streamwise velocity fluctuations (Figure 21) exhibit the typical trend of a turbulent boundary layer with zero pressure gradient [33], with reference fluctuations up to $u'_{rms}/u_\tau = 2.2$ ($u'_{rms}/u_\infty = 0.09$) in proximity of the wall; low reference velocity fluctuations (about $u'_{rms}/u_\infty = 0.006$) are found in the free-stream region ($y/\delta_{99} > 1$), where the flow is nearly uniform. The measured velocity fluctuations show the same trend as the reference ones. However, the fluctuations root-mean-square is slightly overestimated ($u'_{rms}/u_\infty \cong 0.01$) in the free-stream region due to random noise in the measured velocity fields. The overestimation is larger in the near wall region ($y/\delta_{99} < 0.2$, u'_{rms}/u_∞ overestimated by 0.04) due to the limited spatial resolution of the measurement system and to laser light refelctions not completely removed in the pre-processing phase.
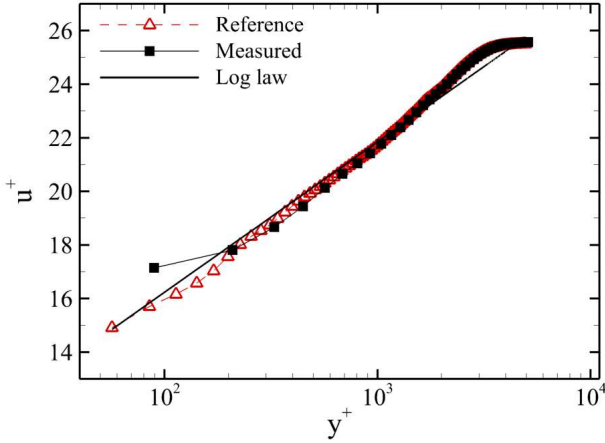
Figure 20. Mean boundary layer profile in inner units; reference data (hollow triangles) and measurement data (full squares).
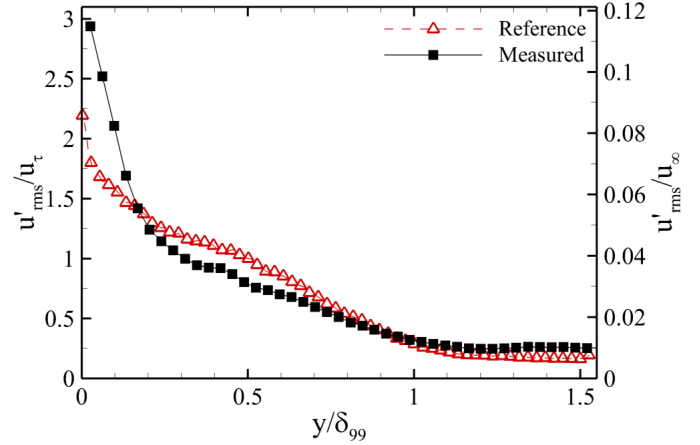

Figure 21. Velocity fluctuations in the boundary layer; reference data (hollow triangles) and measurement data (full squares). For clarity, every three reference data point is displayed.

The measurement error is evaluated both from the difference between measured and reference velocity and with the image matching approach. The error is expected to be the minimum in the free-stream region, where the flow is uniform, and to grow in the wall-normal direction due to the larger velocity fluctuations.

Figure 22 shows an instantaneous velocity profile in the boundary layer with the error bars computed with the image matching approach. As predicted, in the free-stream region measured and reference velocity coincide and the estimated error is few hundredth of a pixel. In contrast, close to the wall the discrepancy between reference and measured velocity becomes evident and the estimated error exceeds 0.2 pixels. For the measured profile, the reference velocity is within the range $[u - \hat{\delta}, u + \hat{\delta}]$ for 85% of the vectors.

The plots of Figure 23 showing the root-mean-square error profiles confirm that the error along the boundary layer follows a trend similar to the velocity fluctuations, being the minimum in the free-stream region ($\delta_{RMS}/u_\infty = 0.01$) and the maximum in the vicinity of the wall ($\delta_{RMS}/u_\infty = 0.07$). The image matching estimation reproduces the same trend as the actual error; however, close to the wall the maximum error is underestimated of about 30%. This *"clipping"* of the estimated error may be attributed to inadequate particle image detection and pairing in presence of large disparities exceeding one pixel.
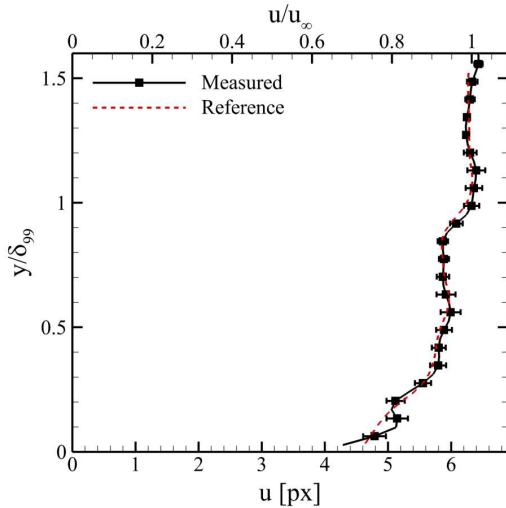

Figure 22. Instantaneous reference and measured velocity profile with error bars in the boundary layer. For clarity, every other data point is displayed.
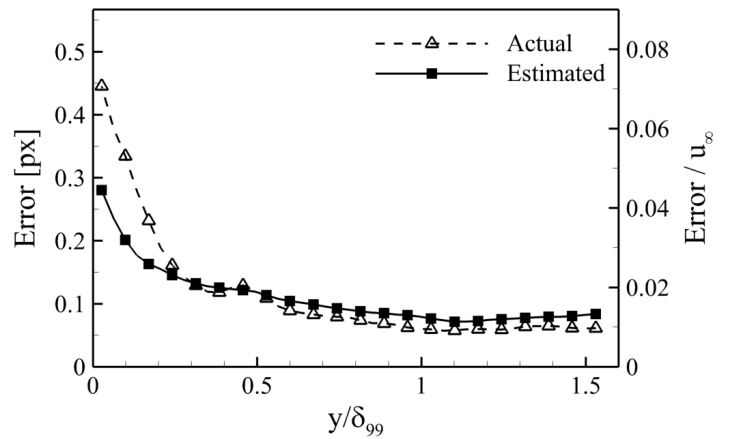

Figure 23. Actual and estimated RMS error profiles in the boundary layer. For clarity, every other data point is displayed.

4.5 Universality proof

To prove the universality of the image matching approach, the uncertainty of the velocity fields from all the experiments discussed in the previous section is examined here; these experiments cover a gamut of flow regimes considered representative of typical PIV measurements.

The cumulative histograms of the actual error δ (Figure 24) show how the measurement error depends on flow regime, imaging conditions and processing parameter. The value 0.1 pixels often considered the typical uncertainty of PIV measurements is far from beeing "universal": in some experiments (e.g. uniform transverse flow with w/δz = 0.02 and 16×16 pixel interrogation window) 80% of the vectors have actual error below 0.1 pixels, while in others (e.g. uniform transverse flow with w/δz = 0.17 and 16×16 pixel interrogation window) the error of more than 70% of the vectors exceeds this value.
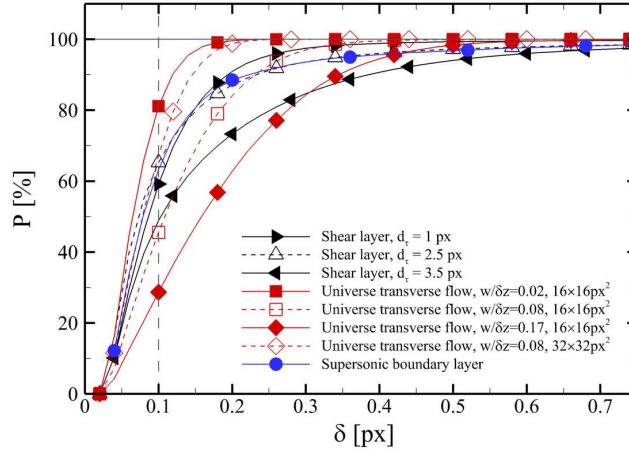

Figure 24. Cumulative histograms of the actual error.

As discussed in section 2.1, both the difference between estimated and actual error (*absolute error discrepancy* ε) and the normalized difference between the two quantities (*relative error discrepancy* ε^*) are monitored to investigate the universality of the uncertainty estimation; for the relative error discrepancy, the normalization factor is chosen to be the absolute value of the local actual error. The cumulative histograms of the error discrepancy (Figure 25) are computed excluding the vectors with actual error below 0.03 pixels, which is the *fog level* regarded to as the sensitivity of the image matching algorithm. Error discrepancies below the fog level fall within the uncertainty of the error estimator.
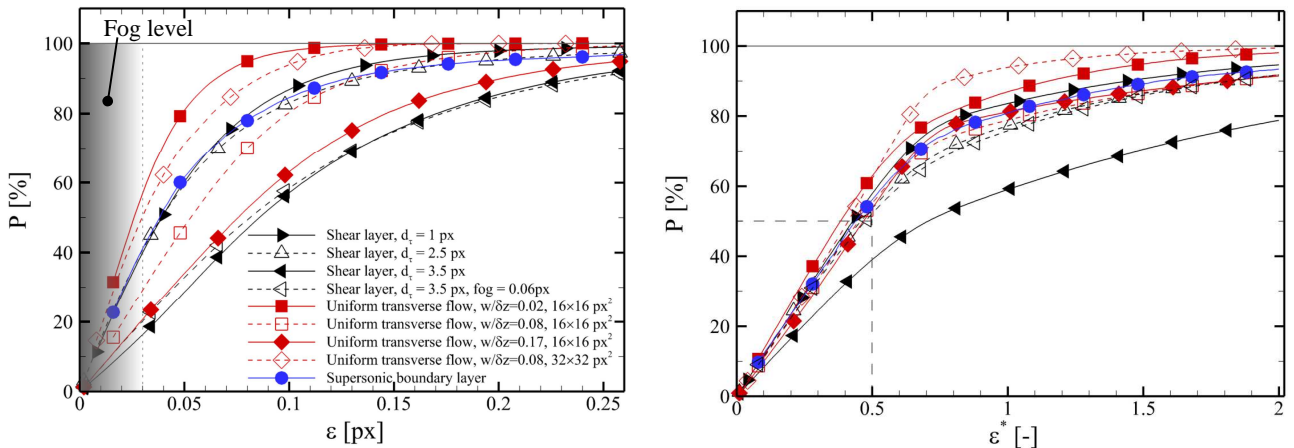

Figure 25. Cumulative histograms of the absolute error discrepancy (left) and of the relative error discrepancy (right). The symbol key applies to both plots.

When plotting the population of vectors against the absolute error discrepancy (Figure 25, left), it is clear that different experimental conditions yield different discrepancy between actual and estimated error. For

example, in experiments with large measurement errors (e.g. shear layer experiement with $d_\tau = 3.5$ px and uniform transverse flow with $w/\delta z = 0.17$ and interrogation window of 16×16 px^2) only 30% of the vectors have error discrepancy below 0.05 pixels, while the percentage rises to 80% in experiments with low measurement errors (e.g. uniform transverse flow with $w/\delta z = 0.02$ and interrogation window of 16×16 px^2).

In contrast, when the relative error discrepancy is considered instead of the absolute error discrepancy (Figure 25, right), the spread of the histograms is strongly reduced. This result indicates that the performance of the image matching error estimator is rather independent of flow regimes, experimental conditions and processing parameters. In detail, the error is estimated within 50% of its actual value for more than 50% of the vectors. The only test case that shows lower accuracy in the uncertainty estimation is the shear layer case with large particle images ($d_\tau = 3.5$ pixels): in these imaging conditions, the estimation of the particle image position is strongly affected by noise and leads to a lower accuracy of the error estimator, as discussed in section 4.1.1. A major improvement of the uncertainty estimation for large particle images is expected with a more advanced particle position detection, e.g. through a two-dimensional 5×5 Gaussian fit instead of the conventional 3-point Gaussian fit [32]. Repeating the calculation of the cumulative histogram only with actual errors above 0.06 pixels, which is justified by the higher fog level for these imaging conditions, the curve of this test case aligns with the other curves (dashed curve with left facing triangles).

5   Conclusions

This work investigates the *universality* of the image matching approach for uncertainty quantification of PIV data, introduced by Sciacchitano *et al* [1]. The approach is assessed using an experimental database that reproduces flow and imaging conditions representative of typical PIV experiments. The analyzed flow fields include laminar shear layer and transition to turbulent regime, turbulent wake behind a bluff body, uniform flow with out-of-plane motion and supersonic turbulent boundary layer. Also the effect of the image defocusing on the measurement accuracy is investigated. Finally the influence of a processing parameter such as the interrogation window size is scrutinized.

The experimental assessment of the uncertainty quantification approach requires the knowledge of the exact measurement error, which is retrieved either with a more accurate measurement conducted by a *high dynamic range system* or by physical considerations on the velocity field and the frequency spectrum. In all the measurement conditions, the image matching approach estimates the RMS error within 30% of the actual value. Measurement errors below 0.05 pixels are typically overestimated due to an intrinsic limit of the approach ascribed to the uncertainty in determining the particle image position with subpixel accuracy.

To discuss the universality of the method, the relative discrepancy between actual and estimated error is considered. Cumulative histograms are plotted which represent the population of vectors having a relative error discrepancy below a given value. It is found that when the error discrepancy is normalized with respect to the absolute value of the local actual error, the population curves spread is strongly reduced, which indicates that the estimator performance are rather independent of flow and imaging conditions and of the selected processing parameters. For more than 50% of the vectors the error is estimated within 50% of its actual value.

REFERENCES

[1] Sciacchitano A, Wieneke B and Scarano F "PIV uncertainty quantification by image matching" Meas. Sci. and Technol. **24** (2013) 045302 (16pp)

[2] Fincham AM and Delerce G "Advanced optimization of correlation imaging velocimetry algorithms" Exp. Fluids **29** (2000) S13-22

[3] Westerweel J "Fundamentals of digital particle image velocimetry" Meas. Sci. Technol. **8** (1997) pp. 1379-1392

[4] Willert CE and Gharib M "Digital particle image velocimetry", Exp fluids **10** (1991) 181-193

[5] Westerweel J "Efficient detection of spurious vectors in particle image velocimetry data sets" Exp. Fluids **16** (1994) 236–47

[6] Westerweel J and Scarano F "Universal outlier detection for PIV data" Exp. Fluids **39** (2005) 1096–100

[7] Westerweel J "Theoretical analysis of the measurement precision in particle image velocimetry" Exp Fluids **29** (2000) pp. S3–S12

[8] Westerweel J "On velocity gradients in PIV interrogation" Exp. Fluids **44** (2008) 831–42

[9] Scarano F and Riethmuller ML "Advances in iterative multigrid PIV image processing" Exp Fluids **29** (2000) pp. S51–S60

[10] Lecordier B, Demare D, Vervisch LMJ, Réveillon J and Trinité M, "Estimation of the accuracy of PIV treatments for turbulent flow studies by direct numerical simulation of multi-phase flow", Meas. Sci. and Technol. **12** (2001) 1382

[11] Nogueira J, Leucona A, Nauri S, Legrand M and Rodríguez PA, "Multiple Δt strategy for particle image velocimetry (PIV) error correction, applied to a hot propulsive jet", Meas. Sci. Technol. **20** (2009) 074001 (11pp)

[12] Nogueira J, Leucona A, Nauri S, Legrand M and Rodríguez PA, "Quantitative evaluation of PIV peak locking through a multiple Δt strategy: relevance of the rms component" Exp Fluids. **51** (2011) pp. 785–793

[13] Timmins BH, Wilson BW, Smith BL and Vlachos PP "A method for automatic estimation of instantaneous local uncertainty in particle image velocimetry measurements" Exp Fluids **53** (2012) pp. 1133–1147

[14] Wilson BM and Smith BL, "Taylor-series and Monte-Carlo-method uncertainty estimation of the width of a probability distribution based on varying bias and random error", Meas. Sci. Technol. **24** (2013) 035301 (11pp)

[15] Wilson BM and Smith BL, "Uncertainty on PIV mean and fluctuating velocity due to bias and random errors", Meas. Sci. Technol. **24** (2013) 035302 (15pp)

[16] Charonko JJ and Vlachos PP "Estimation of uncertainty bounds for individual PIV measurements from cross correlation peak-ratio" Meas. Sci. Technol. (2013) submitted

[17] Eckstein A and Vlachos PP "Digital particle image velocimetry (DPIV) robust phase correlation" Meas. Sci. Technol. **20** (2009) 055401

[18] Wang YQ, Sutton MA, Bruck HA and Schreier HW "Quantitative Error Assessment in Pattern Matching: Effects of Intensity Pattern Noise, Interpolation, Strain and Image Contrast on Motion Measurements", Journal of Strain (2009) **45** 160–178

[19] Tennekes H and Lumley JL "A first course in turbulence" The MIT Press (1972)

[20] Ghaemi S, Ragni D and Scarano F "PIV-based pressure fluctuations in the turbulent boundary layer" Exp Fluids (2012) **53** 1823–1840

[21] Raffel M, Willert CE and Kompenhans J "Particle image velocimetry – A practical guide", Springer, New York (1998)

[22] Keane RD and Adrian RJ "Theory of cross-correlation analysis of PIV images" Appl. Sci. Res. **49** (1992) 191–215

[23] Ragni D, Schrijer FFJ, van Oudheusden BW and Scarano F "Particle tracer response across shocks measured by PIV" Exp Fluids **50** (2011) 53–64

[24] de Kat R, van Oudheusden BW and Scarano F "Instantaneous planar pressure field determination around a square-section cylinder based on time-resolved stereo-PIV", 14th Int Symp on Applications of Laser Techniques to Fluid Mechanics, Lisbon, Portugal, 07–10 July, 2008

[25] De Groot MH "Probability and Statistics" Addison-Wesley publishing company (1989) 2nd edition

[26] Overmars EFJ, Warncke NGW, Poelma C and Westerweel J "Bias errors in PIV: the pixel locking effect revisited", 15th Int Symp on Applications of Laser Techniques to Fluid Mechanics, Lisbon, Portugal, 05–08 July, 2010

[27] Nobach H and Honaken H "Two-dimensional Gaussian regression for sub-pixel displacement estimation in particle image velocimetry or particle position estimation in particle tracking velocimetry", Exp Fluids **38** (2005) 511-515

[28] Jeong J and Hussain F "On the identification of a vortex" Journal of Fluid Mechanics **285** (1995) 69–94

[29] Violato D and Scarano F "Three-dimensional evolution of flow structures in transitional circular and chevron jets", Physics of Fluids **23** (2011) 124104

[30] Nobach H and Bodenschatz E "Limitations of accuracy in PIV due to individual variations of particle image intensities", Exp Fluids **47** (2009) 27–38

[31] White FM "Viscous fluid flow" McGraw Hill, New York (2006)

[32] Sun Z, Schrijer FFJ, Scarano F and van Oudheusden BW "The three-dimensional flow organization past a micro-ramp in a supersonic boundary layer", Physics of Fluids **24** (2012) 055105

[33] Klebanoff S "Characteristics of turbulence in a boundary layer with zero pressure gradient" NACA TN-3178 (1954)